Title
Simulations of RF Probes for Endovascular MRI using the Finite Element Method

Author
Poulin, Nathan Daniel

Publication Date
2016

Simulations of RF Probes for Endovascular MRI using the Finite Element Method

by

Nathan D. Poulin

THESIS

Submitted in partial satisfaction of the requirements for the degree of

MASTER OF SCIENCE

in

Biomedical Imaging

in the

GRADUATE DIVISION

of the

UNIVERSITY OF CALIFORNIA, SAN FRANCISCO

[redacted]

Simulations of RF Probes for Endovascular MRI using the Finite Element Method

by Nathan D. Poulin

September 7, 2016

Acknowledgements

I would first like to thank my thesis advisor, Dr. Steven Hetts. It was a pleasure to learn from him and join him in the interventional suite and sit in on procedures–it has been invaluable to this research. He conducts great lab meetings and always makes you feel welcome.

I want to thank Dr. Xiaoliang Zhang for teaching me about MRI hardware, and getting me acquainted with the essential electrical engineering know how. Thanks to Dr. Martin for providing a review and comments on a draft of this work. Thanks to Dr. Saloner; I appreciate your cardiovascular expertise. Thanks to Caroline Jordan, a post doc who has been a great lab partner, and who got me started on the project. She also gave great feedback on a draft of this work.

I cannot forget to thank Ellen Levitan. She has guided me throughout the submission of this thesis and has been very patient with me.

A huge special thanks to COMSOL technical support. I have flooded the tech support team with software questions and they have always been quick to respond with exactly what I need.

And lastly, I cannot thank my family enough for all of their love and support. Thanks Mom, Gabby, Mitch, Pépère, and Grandma. I love you guys and look forward to seeing you soon.

Contents

List of Figures

List of Tables

Abstract

The positioning of surface receiver coils limits the signal-to-noise ratio (SNR) of MRI. Endovascular RF imaging coils placed at or near the region of interest can image at greatly enhanced SNR compared with surface coils. Treatment protocols for neurovascular and cardiovascular diseases and conditions would benefit from better image quality.

A series of numerical simulations using the Finite Element Method (FEM) of the electric and magnetic fields of endovascular RF probes of the looped and loopless (antenna) kinds were performed in order to assess their imaging performances and to improve their designs at the imaging strength of 3T. Safety of the probes was also considered. Emphasis is placed on simulations of a loopless coil, with and without the addition of an extremely high dielectric coating. A new design concept for actively tracking the distal end of a loopless coil is proposed, where signal dropout normally prevents its visualization and localization. This would be one of the few available multi-functional coils which could be used for imaging and tracking. The design consists of a corkscrew shaped inductive loop placed at the end of the loopless coil (maintaining an open circuit), with its axis oriented in the xy plane, allowing for signal gain in the axis of the loop. Electric and magnetic fields were mapped and preliminary SNRs and Specific Absorption Rates (SARs) are presented, showing the corkscrew's viability as a potential active tracking mechanism.

Chapter 1

Introduction

1.1 Clinical Background

With the continuing trend towards minimizing invasiveness, interventional procedures using catheters, guidewires, and associated electrical and mechanical devices are becoming more common [1]. Interventional techniques are most applicable to the treatment of neurovascular and cardiovascular diseases and conditions, such as stroke and heart disease. Additionally, interventional radiology provides treatment options for cancer. However, the work of this thesis will not be concerned with cancer applications. We instead focus on improving endovascular MRI technology for assessing tissue viability within the ischemic penumbra following stroke and for imaging atherosclerotic plaques and surrounding parenchyma. Another potential application of this work could be the micro-anatomical description of dural arteriovenous fistulas, which are currently not easily imaged with conventional diagnostic CT and MRI.

In order to get the catheter to the site of treatment, a sheath is typically inserted into the femoral artery (see Fig.1.1 (a)) for arterial access and x-ray angiography is usually used to

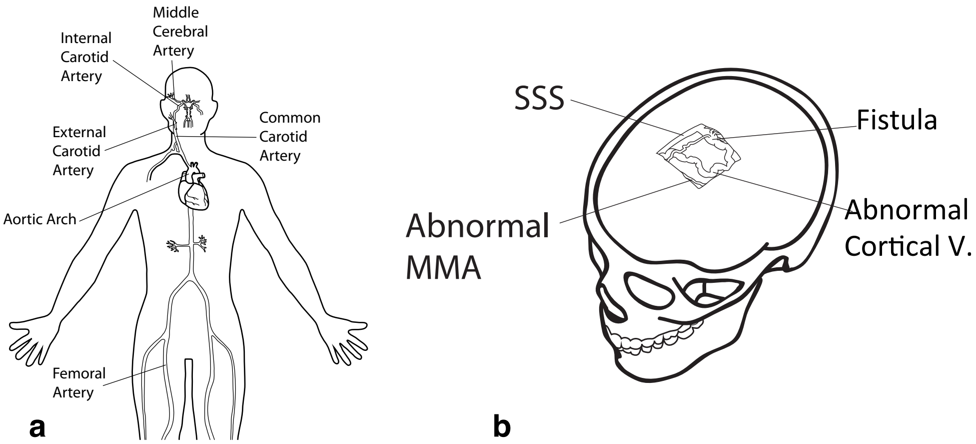

Figure 1.1: Basic anatomy of the vasculature accessed by endovascular instruments (a) and a Borden Type 3 dural arteriovenous fistula, with the abnormal cortical vein containing the fistula at the top right of (b). Illustrations by Jon Chan, with (b) adapted from [2].

guide the catheter, with the flexible and maneuverable guidewire leading and the catheter following close behind. Once the catheter is in place, the guidewire can be removed. This creates a portal into the vascular system. Devices attached to smaller catheters can be quickly inserted through the larger diameter catheter, to be used for thrombolytic therapy for the treatment of stroke, for closing off dural arteriovenous fistulas, for coiling of aneurysms, or for many other treatment options [1, 3].

1.1.1 Pathogenesis of Atherosclerosis

Many texts have expounded on the inflammatory origins of atherosclerosis [4–6]. However, it is important to briefly mention the progression of atherosclerotic plaques and just a couple of the major imaging methods to understand where atherosclerosis fits in with the following technical scheme.

Atherosclerotic plaques consist mainly of three components. The first of these is connective tissue extracellular matrix, composed of collagen, proteoglycans, and fibronectin elastic fibers. Cholesterol containing components, such as crystalline cholesterol, cholesteryl esters, as well as phospholipids make up the 2nd major component. And finally, atherosclerotic plaques contain monocyte-derived macrophages, T lymphocytes, and smooth muscle cells. Early stages of atherosclerosis within the arterial wall are asymptomatic, and involve the proliferation of lipid filled macrophages and the recruitment of inflammatory cells. These cell types coalesce to form an early stage plaque. The plaque first grows in the abluminal direction before encroaching upon the lumen (i.e. stenosis). The expanding plaque can leak its contents, containing tissue factor, initiating the coagulation cascade and consequently, thrombosis. The plaque can reheal with fibrous tissue, pushing the apex of the plaque further into the lumen. Calcification is characteristic of late stage plaques. This process severely malforms and reorganizes the three layers (intima, media, and adventitia) of the arterial wall. Unstable plaques can irreparably rupture, forming a thrombus which entirely occludes the vessel, or breaks off and occludes a smaller vessel downstream.

Better in-vivo methods for imaging arterial plaques are important for a more detailed understanding of the biochemical disease progression. Many of the current imaging modalities are adequate for identifying lumenal diameter, wall thickness, and plaque volume. Diagnosis of coronary, carotid, and peripheral lesions is mostly done with X-ray angiography. Computed tomography (CT) is the best at quantifying calcium volume. The superficial location of the carotid arteries make them more easily imaged with ultrasound and MRI, but deeper arteries are much more difficult to characterize escape. While each of these techniques has their advantages, none of them are good enough for definitive diagnosis of vulnerable plaques and detailed description of their composition [4, 7, 8].

1.1.2 Stroke and the Ischemic Penumbra

There are two main categories of stroke—ischemic and hemorrhagic. Hemorrhagic stroke results from a burst aneurysm or arteriovenous malformation, or tear of a weak vessel.

Ischemic stroke accounts for roughly 88% of all cases [9], resulting from embolic occlusion of a blood vessel in the brain by a dislodged thrombus originating elsewhere in the body (typically the heart) or from thrombotic occlusion, where a thrombus is produced by an atherosclerotic artery in the brain.

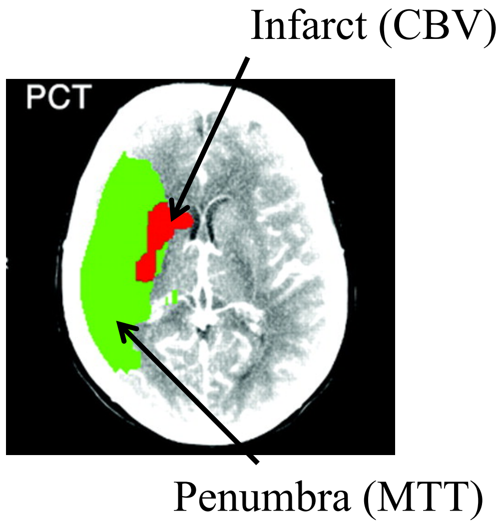

Figure 1.2: Overlay of the MTT map (green) with the CBV map (red) from a perfusion CT study taken 4 hours after symptom onset of a stroke, showing the extent of the regions of ischemic penumbra and infarct, respectively. The subject is a 65 year old man, whose right proximal M1 segment of the right middle cerebral artery (MCA) is occluded. The image is reproduced from [10] with permission.

The diminished blood flow at the onset of an ischemic stroke causes infarction of tissue in the vicinity of the occluded vessel. The region beyond the infarct is called the ischemic penumbra, where collateral circulation is able to maintain just enough perfusion for metabolic function. There is no synaptic transmission in the penumbra, but high enough oxygen levels keep ATP concentrations relatively normal [11]. Areas of infarct are unsalvageable. Recovery of function in the penumbra is possible if it can be properly identified. Understanding where these different regions lie is needed in order to guide treatment. Restoring blood supply to an large infarct can exacerbate the condition, causing hemorrhage and possibly death.

CT-perfusion is one of the best techniques for assessing the ischemic penumbra. Intravenous iodinated contrast material is injected and images are acquired at about 1 frame per second with typically around 50 images acquired for each injection. This allows for a quick imaging session. The Mean Transit Time (MTT) and Cerebral Blood Volume (CBV) are the two most important parameters for mapping regions of infarct and ischemic penumbra. The MTT maps how long it took for blood to get to a certain region of the brain, whereas CBV quantifies how much blood got to that region. The ischemic penumbra will have enough blood flow to survive, at least within some time window, but the blood supply will take longer to reach its destination since it must recruit flow from collateral circulation routes. The infarct core, however, does not receive any blood supply, and CBV is most suited for its detection. The MTT map can be overlaid with the CBV map to visualize the salvageable and non-salvageable regions [12]. The green and red regions in Fig.1.2 show the overlay of MTT and CBV of a 65 year old stroke patient [10]. The red region represents a very low CBV value, indicating the location of infarcted tissue and the green is the area of the ischemic penumbra where the MTT is longer.

Although CT perfusion maps, as discussed, are the go to standard for identifying tissue salvageability, the accuracy of the technique is dependent on the thresholding of the post-processing method [13]. Also, some time will inevitably pass following image acquisition and before the patient undergoes thrombolytic therapy. The perfused regions could change within this timeframe. The infarct could progress into further territories or areas of the ischemic penumbra could be better perfused. Imaging techniques for localizing the ischemic penumbra and infarcted tissue concurrent with the delivery of therapy could aid more accurate and safe treatment.

1.1.3 Dural Arteriovenous Fistulas

The outermost meningeal layer of the brain and spinal cord, the dura mater, can contain pathological contortions of small blood vessels known as dural arteriovenous fistulas (DAVFs). These small vessels act as an unwanted shunt between an artery and vein. Drainage of arterial blood into the vein can cause venous hypertension resulting in neurological deficit, infarct, and possibly hemorrhage [14]. The overall blood circulation throughout the brain can be altered significantly from just one of these lesions. The majority of DAVFs originate spontaneously in adulthood.

DAVFs are anatomically diverse and complex, and the classification schemes of Borden and Cognard are able to identify increased risk of intracranial hemorrhage. These schemes are based on the location of venous drainage, whether or not the flow in the venous sinus is antegrade or retrograde, if cortical venous drainage is present or absent, among other things. A schematic of a type 3 DAVF based on the Borden classification scheme can be seen in Fig. 1.1 (b). Here, the abnormal middle meningeal artery shunts to the cortical vein. The most reliable modality for detecting these lesions is X-ray angiography, but better stratification of symptomatic and asymptomatic lesions could help to single out at risk patients [2]. Sequential images using 4D-CTA is an alternative modality that has been successful at identifying DAVFs, albeit at reduced spatial and temporal resolution when compared to angiographic methods [15]. Depending on their locations, DAVFs could be reached by endovascular MR imaging coils.

1.2 The Need for MRI

Endovascular instruments are typically visualized and navigated to the vasculature of interest under X-ray angiographic guidance. Several drawbacks of this imaging technique constrain the scope of treatment. Continuous exposure of ionizing radiation to the patient poses safety concerns, especially if distant and hard to reach vasculature must be accessed. The imaging region is mostly restricted to the vessel lumen and radiographic projections can distort the image, especially as the lumenal ellipticity increases [16]. There is potential for guiding catheter devices using MRI, since MRI is safe and produces images with exquisite anatomical detail of soft tissues.

In addition, endovascular imaging coils attached to catheters can get closer to internal anatomy, compared with traditional surface coils. This allows for greatly enhanced SNR over the imaging region. This is particularly important for imaging deep arteries, since their

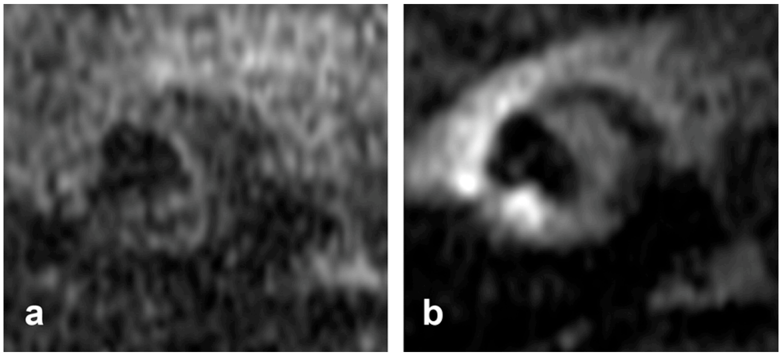

Figure 1.3: Image comparison using a surface coil (a) and an endovascular loopless coil (b). The in vivo images are of a subject's common iliac artery, which contains an atheroma. The images for each coil were obtained with the same imaging parameters (TR, 500 ms; TE, 13 ms; BW, 16 kHz; 9 cm FOV; 256x256 matrix size; no phase wrap; in plane resolution of 316 micron. The SNR using the endovascular coil is greatly enhanced. Reproduced from [17] with permission.

locations preclude detailed tissue characterization using surface coils. An excellent display of the enhanced SNR of an endovascular coil over a surface coil can be seen in Fig.1.3. The image is of an atherosclerotic plaque in the common illiac artery from an in vivo study. The endovascular probe they used is what is called a loopless coil, which is just a length of conducting wire. This type of coil will be described in more detail in a later section. As seen from the side by side comparison of images in Fig.1.3, the endovascular coil is able to resolve the lumen, fibrotic tissue, and calcium deposits, while the surface coil is inadequate in characterizing the atherosclerotic plaque [17].

1.2.1 The MRI Signal and its Reception

In the majority of MRI studies, the generated signal is based on the precessional character of Hydrogen nuclei after being driven with an RF pulse orthogonal to a large static magnetic field B_o. The precessional frequency, also known as the Larmor frequency is given by $\omega = \gamma B_o$ with γ the gryomagnetic ratio. A more in depth understanding of the origin of spin angular momentum and the MRI signal requires derivation via quantum mechanics, but for our purposes, a more succinct description of the phenomena will suffice. The results are presented so as to lead towards the positional dependence of the receiver coil on the SNR, and is largely adapted from [18].

The equilibrium magnetic dipole density M_o is an important quantity. It describes the bulk magnetic moment of spins when subject to B_o and is given by:

$$M_o = \frac{\rho_o \gamma^2 \hbar^2}{4kT} B_o \tag{1.1}$$

where ρ_o is the number of spins per unit volume (spin density), k is Boltzmann's constant, T is the absolute temperature, and $\hbar = h/2\pi$, where h is planck's constant. The precessing magnetization after being tipped by an RF pulse, creates a time varying flux ϕ in the coil and thus, an electromotive force (emf) by Faraday's law of induction:

$$emf = -\frac{\mathrm{d}}{\mathrm{d}t}\phi(t) \tag{1.2}$$

From the principle of reciprocity, eq. 1.2 can be rewritten as the following integral over the volume of the sample:

$$emf = -\frac{\mathrm{d}}{\mathrm{d}t}\int_{sample} d^3r \vec{M}(\vec{r},t)\vec{B}^{receive}(\vec{r}) \tag{1.3}$$

where r is composed of x, y, and z directions, $\vec{B}^{receive}$ is the magnetic field produced by the receive coil per unit current and $\vec{M}$ is the precessing magnetization. The principle of reciprocity [19] says that the inductive coupling of the coil with the magnetization is equivalent to a unit current flowing in the receive coil. Eq. 1.3 can help us understand why getting closer to the magnetization of interest or imaging region with the receive coil, enables higher signal gain. This is because the inductive effect is positionally sensitive. The received signal is directly related to the emf and depends on the position of the receive coil with respect to the precessing magnetization.

The role reversal effect from the principle of reciprocity allows us to simulate coils by supplying them with a voltage or current source. In this way, the EM fields generated by the coil, especially given simple coil geometries, are nearly the same as the fields produced from an induced emf in the coil from the sample magnetization. Put another way, the reception and transmission profiles are similar.

1.3 Endovascular RF coils

There are two main types of endovascular imaging coils which have developed in parallel– those that are looped [20] and loopless. The looped coil that studied here is called a transmission line resonator. It is a simple structure, and consists of a single or double turn loop made of the inner conductor of a coaxial cable. The loop is shorted by the outer conductor of the coax. This design maximizes current flow in the loop, while minimizing voltage. The coil provides an elevated SNR in the region of the loop, as well as minimal thermal deposition from the electric field. However, the SNR falls off quickly beyond the region of the loop [21]. In addition, access to smaller vessels requires an increasingly smaller loop. This inevitably reduces the imaging coverage.

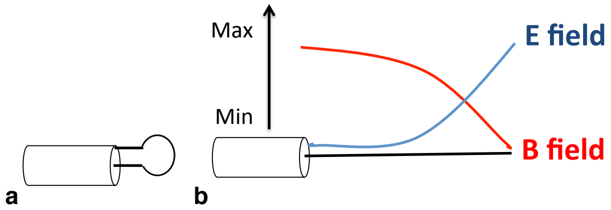

Figure 1.4: Schematic diagrams of the Transmission line resonant coil (a) consisting of a single turn, shorted loop as well as a loopless coil (b)

On the other hand, the loopless coil's simple geometry make it possible to access small arteries and veins without compromising the imaging coverage or performance. The first loopless imaging coil, or antenna, as named by its inventors, was developed by Ocali and

Atalar [22] nearly 20 years ago. It can be understood simply as a wire measuring a quarter wavelength, acting effectively as a dipole 'antenna'. With this configuration, the magnetic field is maximal at the proximal end and zero at the distal end, with the reverse relationship for the electric field, seen in Fig. 1.4. The advantages of the loopless coil are that it has an extended imaging coverage at the proximal end irrespective of any particular coil orientation. This makes it well suited for endovascular imaging, since a guidewire can be engineered to behave as a loopless coil [23]. However, the decaying magnetic field and increasing electric field along its length make a considerable portion of its distal end virtually invisible. This is a serious problem if the goal is to eventually use the device in the clinic, and the signal dropout is explained in more depth in a following section.

Antenna or Coil?

When reading the literature, one can get confused as to the meaning of certain terms. The imaging coil consisting of a single short piece of conducting wire that measures some multiple of a quarter or half wavelength was originally referred to as an 'antenna' or 'loopless catheter coil'. Typically, the term 'antenna' is reserved for structures which radiate or receive a signal in the far-field domain, where the radiative EM field dominates over the near-field, or reactive field.

More generally, the wavelength of any electromagnetic wave is influenced by the medium that it travels within, given by $\lambda = c/f = 1/f\sqrt{\mu\epsilon}$ where λ is the wavelength, f is the frequency, μ is the permeability of the medium, and ϵ is the permittivity of the medium. The ratio of the EM wave components, E/H, where H is the magnetizing field ($B = \mu H$), is known as the wave impedance η. This ratio can help us understand the difference between the near field and far-field regions. The equilibrium wave impedance η_{medium} $(= \sqrt{\mu/\epsilon})$ is given by the material property. For a piece of wire connected to an AC Voltage source, the magnetic field generated by the wire will be much larger than the electric field in the wire's vicinity, and thus, $\eta < \eta_{medium}$. This behavior is restricted to the near field region. With increasing distance from the wire, the magnetic field drops off at a faster rate than the radiative component, and the wave impedance transitions to the equilibrium wave impedance–the end of this transition marks the beginning of the far field region, where the EM wave propagation is purely radiative [24].

For our endovascular applications at 3T, with the goal of imaging blood vessels and surrounding tissue, the imaging location resides in the near field. For this reason, we call our wire a 'coil'. We also refer to our coils as 'probes'.

Signal dropout of the loopless coil

One of the main issues with the loopless coil is its signal dropout at the distal end. Several factors account for this. The quarter wave nature of the probe, with a large impedance mismatch between the probe tip and tissue, prevent electromagnetic wave propagation. Thought another way, current flow has to terminate, since the circuit is left open. Furthermore, the noise resistance increase towards the distal end worsens the problem. If the coil is to be used for endovascular MRI, then one needs to be able to know precisely where the tip resides. If angiographic guidance is used to navigate the coil to a region to be imaged with MRI, the patient will then have to be lifted and transported to the MRI scanner. This will compromise the location of the probe–an obvious safety hazard.

Studies have been done to try to regain signal at the end of the loopless coil. The loopless coil is usually covered with insulation for in vivo studies. This is needed to prevent electric currents from being in direct contact with human tissue. This has the unwanted effect of increasing the pole length, since the dielectric constant of the insulation is usually much less than soft tissue and blood. The distal sensitivity is also compromised even more than for a bare antenna. Tapered insulation with decreasing thickness towards the tip can slightly improve the distal sensitivity [25]. This acts by pushing current flow further down the pole length. Even given these attempts, signal recovery at the distal tip has not been adequate.

Circuit considerations

There are two main types of resonators, consisting of resistive, capacitive and inductive components (RLC). The two types–series and parallel, are based on the arrangements of the RLC components. Our receive probes are effectively series RLC circuits, with the distributed inductance and capacitance arranged in a linear fashion. We briefly describe the series RLC circuit here, similar to [26]. The impedance of the series RLC resonator is:

$$Z = r + jL\omega + \frac{1}{jC\omega} = r + j\left(L\omega - \frac{1}{C\omega}\right) \tag{1.4}$$

The resonant condition is reached when the capacitive component of the impedance is equivalent to the inductive impedance:

$$L\omega_o = \frac{1}{C\omega_o} \tag{1.5}$$

This occurs for one frequency:

$$\omega_o = \frac{1}{\sqrt{LC}} \tag{1.6}$$

When the probe is tuned to the resonant frequency, the energy exchanges between the inductive and capacitive components and slowly dissipates in the resistive component.

The total resistance is given by:

$$r = r_\Omega + r_M + r_E + r_R \tag{1.7}$$

where r_Ω is the resistance of the metallic parts, r_M accounts for magnetic losses from the induced (eddy) currents in the conductive sample, r_E is the electric loss from the electric field generated by the probe, and r_R is the far-field radiative loss which is negligible. It is important to have these different loss effects in mind when designing an RF probe.

The easiest way to tune the probe to the desired resonant frequency is to use a network analyzer. The loopless coil is essentially a 1-port network. A schematic of a 1-port network is shown in Fig. 1.5. The S11 parameter can be measured, which is just the ratio of the amplitude of the signal that reflects from the port to the amplitude of the signal incident on the port.

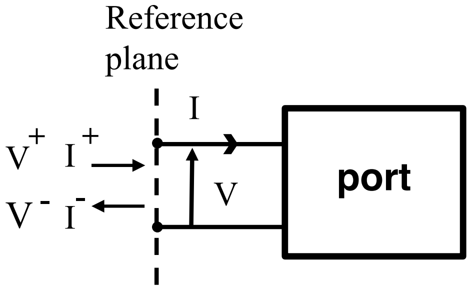

Figure 1.5: Schematic of a 1-port network.

The voltage and current, described by components transmitted from the port to the probe and reflected from the probe back to the port are given by:

$$\begin{aligned} V &= V^+ - V^- \\ I &= I^+ - I^- \end{aligned} \tag{1.8}$$

where V^+ and I^+ are the incident voltage and current and V^- and V^- are the reflected voltage and current.

The reflection coefficient is given by:

$$\Gamma = \frac{V^-}{V^+} = \frac{Z - Z_o}{Z + Z_o} \tag{1.9}$$

where $Z = V/I$ is the impedance of the probe and Z_o is the characteristic matching impedance of 50 Ω. Tuning of the frequency is done by changing the capacitance and inductance of the probe and transmission line, either by use of a variable capacitor or by cutting off lengths of the transmission line. The procedure for doing this with simulations is analogous, and will be described in Chapter 2.

Dielectric Properties

The highly conductive and lossy sample loading conditions of the human body need to be considered when running EM simulations of endovascular coil performance. The human body can be viewed as a dielectric material, and the 'displacement' electric field set up in this dielectric is:

$$\vec{D} = \epsilon \vec{E} \tag{1.10}$$

with the permittivity ϵ of the sample, and $\vec{E}$ the electric field produced by the probe . The permittivity is a value that has an imaginary component:

$$\begin{aligned} \epsilon &= \epsilon' - j\epsilon'' \\ \epsilon' &= \epsilon_o \epsilon_r \end{aligned} \tag{1.11}$$

with the real part ϵ' and imaginary component ϵ'', the relative permittivity ϵ_r, also called the 'dielectric constant' and ϵ_o the permittivity of vacuum. The imaginary component results from the delayed response or polarization of the material to the applied alternating electric field. This phase offset is the source of electrical heating and the r_E term in eq. 1.7. These electrical losses are dependent on the loss tangent or phase angle:

$$tan\delta = \frac{\epsilon''}{\epsilon'} \tag{1.12}$$

The loss tangent is dependent on the sample medium, and this value varies widely for different tissues. The permittivity is actually highly dependent on the driving frequency and conductivity of the sample. The values for biological tissue contain 4 dispersion regions. This is better understood from the Cole-Cole expression for the permittivity, which ranges from Hz to GHz [27]:

$$\epsilon(\omega) = \epsilon_\infty = \sum_{n=1}^{4} \frac{\Delta\epsilon_n}{1 + (j\omega\tau_n)^{(1-\alpha_n)}} + \frac{\sigma_i}{j\omega\epsilon_o} \tag{1.13}$$

where ϵ_∞ is the permittivity in the terahertz regime, σ_i is the ionic conductivity, τ is the relaxation time for each dispersion region, and $\Delta\epsilon$ is the drop in permittivity in the range of $1 >> \omega\tau >> 1$. This model described by eq. 1.13 can be used to extract the permittivity values for each tissue at the desired frequency.

The standard value for assessing coil safety in the body is the Specific Absorption Rate [24] in W/kg, given by:

$$SAR = \sigma_i \frac{|E|^2}{\rho} \tag{1.14}$$

where ρ is the mass density in Wkg^{-1}, and E is the rms electric field in Vm^{-1}. This quantity measures power deposition in tissue from the electric fields of the probe, and it can be much more easily simulated then measured experimentally.

1.4 COMSOL and the Finite Element Method

Numerical techniques for reaching otherwise intractable solutions to nonlinear partial differential equations have had widespread use in many disciplines of science and engineering, and the Finite Element Method (FEM), specifically, has had great success. We utilize COMSOL Multiphysics (Stockholm, Sweden), a software package based on the FEM that allows the user to build and simulate models with complex geometries, initial values, and boundary conditions [28]. The FEM is based on discretizing the geometrical domain into an array of shapes called the *finite elements*, which simplifies the mathematical problem. A system of equations can be assembled to derive a description, or approximation, of the whole system. For our electromagnetic applications, Maxwell's wave equations are numerically approximated.

1.4.1 Error analysis of a 1D analytical solution

Although the FEM is widely accepted as an excellent technique for approximating solutions, it is worth comparing an analytical solution of a simple differential equation with results of a COMSOL simulation. We consider a 1-D boundary value problem on the interval x, spanning 0 to 2π. The interval is split up into N_e line segments or *finite elements*, where $N_e = N_n - 1$ with N_n the number of nodes, seen in Fig.1.6. The following is a linear, second order ordinary differential equation:

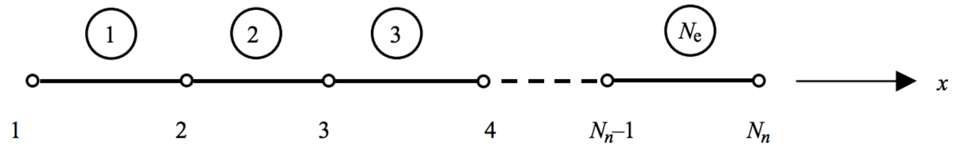

Figure 1.6: Discretization of the 1-D interval, with the number of finite elements N_e and the number of nodes N_n. Reproduced from [29].

$$\frac{d^2u}{dx^2} + \frac{du}{dx} + u(x) = 2\cos(x) + x + 1 \tag{1.15}$$

with x, the independent variable and u the dependent variable. We should note that eq. 1.15 does not represent a physical situation. The general analytical solution of eq. 1.15 is:

$$u(x) = C_1 e^{-x/2} \sin\left(\frac{\sqrt{3}}{2}x\right) + C_2 e^{-x/2} \cos\left(\frac{\sqrt{3}}{2}x\right) + x + 2\sin(x) \tag{1.16}$$

where C_1 and C_2 are constants. After applying the following boundary conditions: $u(0) = 0$ and $u(2\pi) = 2\pi$, on the interval $0 \leq x \leq 2\pi$, the general analytical solution reduces to:

$$u(x) = x + 2\sin(x) \tag{1.17}$$

The plot of $u(x)$ vs. x can be seen in Fig.1.7 (a).

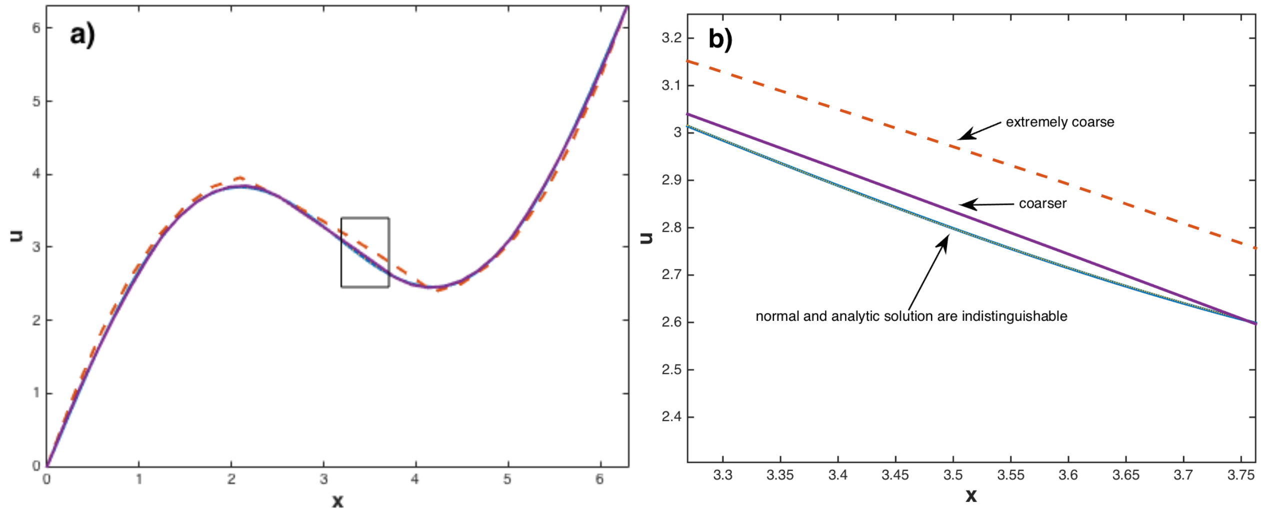

Figure 1.7: The analytical solution of equation 1.15 is plotted as u vs. x in (a) with COMSOL FEM simulations from 3 different mesh refinements: extremely coarse, coarser, and normal. A zoomed in view (b) shows the degree to which the FEM can approximate the analytic solution for different mesh settings.

COMSOL simulations of eq. 1.15 with the appropriate boundary conditions were run for nine different mesh refinements: extremely coarse, extra coarse, coarser, coarse, normal, fine, finer, extra fine, and extremely fine. These mesh settings have N_e's equal to 21, 35, 56, 70, 105, 133, 162, 200, and 300, respectively. The extremely coarse, coarser, and normal simulations are included in the plot of the analytical solution, seen in Fig.1.7 (a). Notice in Fig. 1.7(b) how the normal mesh simulation is indistinguishable from the analytical solution when zoomed in approximately 10x. We can quantify the error by normalizing the difference of the area under the analytic curve with the areas under the numerical curves, given by the following:

$$error(\%) = \left\{ \frac{1}{|A_{Exact}|} \sum_{e=1}^{N_e} |A^e_{Exact} - A^e_{Numerical}| \right\} 100\% \tag{1.18}$$

where A_{exact} is the area under the analytic curve and $A_{Numerical}$ is the area under the numerical curve. The percent error for each mesh refinement can be seen in table 1.1. Even the coarse mesh refinement with 70 finite elements only has a percent error of 3.7×10^{-4} which is a negligible error for most applications.

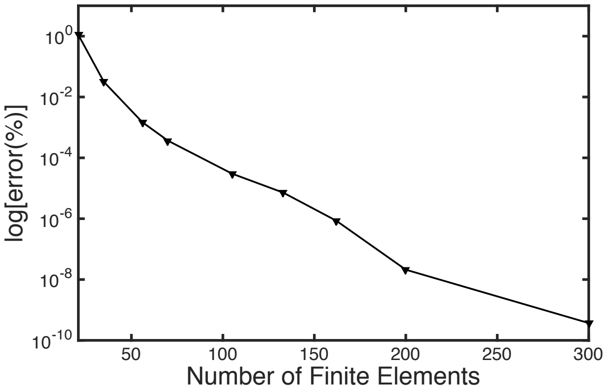

Figure 1.8: Plot of the percent error (on a log scale) of different mesh refinements with varying numbers of finite elements.

Table 1.1: Numerical percent error values for different finite element numbers.

Number of finite elements	% error
21	1.1039
35	0.0312
56	0.0015
70	3.7×10^{-4}
105	3.0×10^{-5}
133	7.2×10^{-6}
162	8.6×10^{-7}
200	2.1×10^{-8}
300	3.7×10^{-10}

Although complex geometries and electromagnetic configurations highly complicate this simple example, such that analytic solutions of Maxwell's equations do not exist, it nonetheless validates the FEM as an accurate solver.

Chapter 2

RF Probe Simulations

Simulation of RF probes is an invaluable method for obtaining detailed electromagnetic information that is otherwise very difficult to get with bench tests and imaging studies. Once the user becomes proficient with the software of choice, quick builds and subsequent simulation tests can be used to improve designs. In vivo studies using endovascular RF coils require a lot of resources and effort. Complicated sample loading conditions from the human or animal body can be included in the simulations at no extra cost. The simulation results can help to quickly discard bad ideas, and prompt benchwork and further recruitment of resources and effort for good ideas. It helps to have a reliable estimate of how your device will behave rather than starting from scratch on the bench.

The series of simulations using COMSOL Multiphysics that follow explore the electromagnetic performance of a transmission line coil, a loopless coil with and without extremely high dielectric coating, and a new corkscrew loop which could potentially be used to track the distal tip of a loopless coil.

2.1 Setting up the simulations

The basic workflow in COMSOL begins with setting up the physics module(s) for the specific application, followed by building the geometry. The simulation environment in COMSOL is restricted to a spherical domain with a perfectly matched layer (PML). This prevents all electromagnetic waves radiating outward from reflecting at the interface between the PML and the environment of the model, whether that be air, water, or tissue. The simulation geometry, however, does not need to be made identical to what would be used in a physical experiment. Including additional electrical components and lengths of wire complicate the simulation, and could disappoint the user when they find that the solution does not converge. For the loopless coil, the geometry consists of a lumped port which supplies the AC Voltage, a length of wire measuring approximately a quarter wavelength, and a ground plane with the side closest to the lumped port modeled as a perfect electric conductor. Most of the conducting components are modeled as perfect electric conductors, with the exception of a simulation of the reflection coefficient in sec. 2.2. Again, this not only streamlines the simulation, but it also allows for an understanding of how the device would operate without 'ohmic' or metallic losses from the device. In reality, the length of the wire connecting to the coil would be in the meter range, and would be connected to a tuning/matching circuit before being connected to the scanner. Since resonant conditions are periodic in nature, this allows us to simplify the situation without losing confidence in the accuracy of the results.

Given the relatively fast computation time afforded by COMSOL and complicated set-up of the physics, it is prudent to start the simulations with a very simple case and make small changes in an iterative fashion. This may seem obvious, but when multiple applications are tested in parallel, it is easy to forget where one may have left something out. After creating the geometry, the electromagnetic boundary conditions and sample loading conditions must be set up. This involves the creation of a lumped port for an AC Voltage, selection of the PECs, and assignment of materials with the appropriate dielectric properties. As indicated

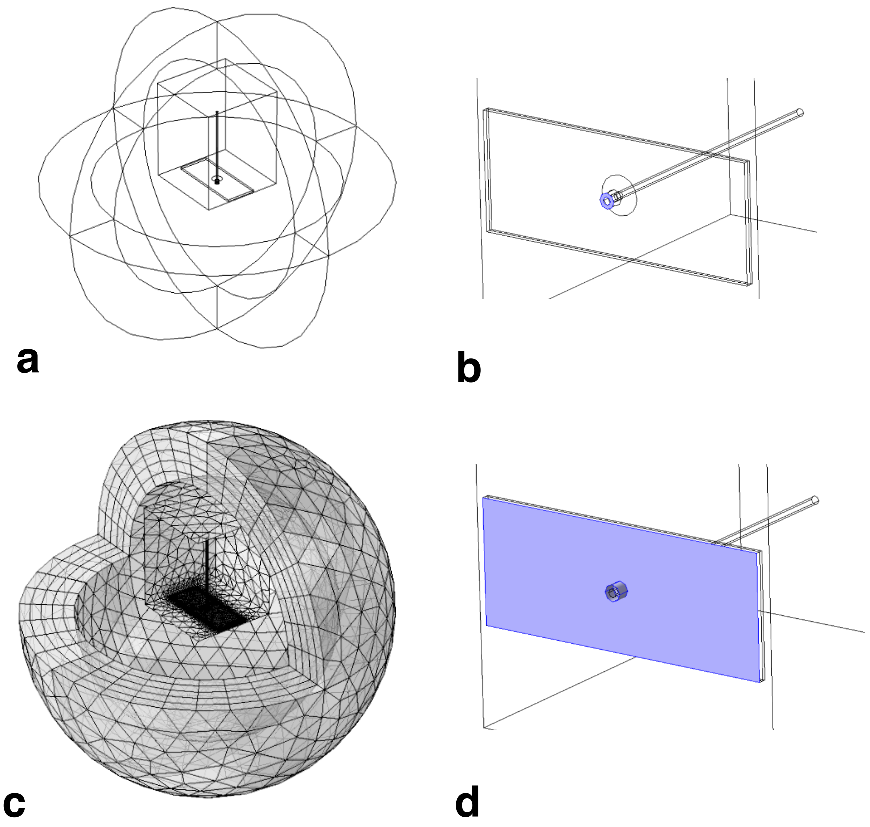

Figure 2.1: Wireframe rendered geometry of the entire domain (a), the highlight of the lumped voltage port (b), the highlight of the perfect electric conductors (d), and the discretization of the geometry into finite elements following mesh generation (c). Different domains within the geometry are assigned different shapes and refinements

.

in section 1.3, care must be taken when considering the sample loading conditions. The simulation will not produce desirable results if the imaginary component of the permittivity of the sample is not included. This is especially true for media with large loss tangents, such as highly conducting tissues of the body.

A wireframe rendering of the geometry for the loopless coil can be seen in Fig. 2.1 (a). The cube within the spherical domain has the dielectric properties of blood, with a relative permittivity of 73 with an imaginary component of 175, a relative permeability of 1 and a conductivity of 1.25 S/m. The entire domain was not made of blood for two reasons. First, the highly conductive medium will cause leakage of currents at the voltage port. The second reason is because the conductive medium around the uninsulated loopless coil will short the circuit. In reality, all in vivo studies would require an insulating material. The cube of blood bisects the thickness of the ground plane, which is made up of a dielectric material with no conductivity. The rest of the domain is modeled with the same permittivity and permeability as blood but with a conductivity of 0. Fig. 2.1 (b,d) shows the highlights in blue of the lumped port and ground plane, respectively. The mesh generation over the simulation domain can be seen in Fig. 2.1 (c), with the PML being the outermost layer.

The probes were designed to operate at 128 MHz for 3T MRI. The length of the loopless coil was estimated by $\lambda/4 = c/(4f) = \lambda/(4f\sqrt{\epsilon})$. This involves numerous parametric sweeps over lengths and frequencies. We used a quad core computer, and ran batch sweeps, where 4 processes can simulate in parallel. This greatly reduced the computation time. All probes were excited with 1V at the resonant frequency.

2.2 Simulating the Reflection Coefficient

When running these simulations, it is easy to ignore validation of the reflection coefficient. There is no alert, or error that points you in the right direction when it comes to making sure your resonant structure is actually resonating. And with each minor change to the structure, one needs to make sure they have not strayed too far from the resonant peak. If the reader is familiar with COMSOL, they may know that S11 is a derived value. However, when simulating, one typically solves for a single frequency value. This usually takes around 1-10 minutes. To create a full plot of S11, a parametric sweep over a range of frequencies must be carried out. This can take anywhere from 30 minutes to several hours, depending on the sample loading conditions.

Loopless coils were simulated with a range of lengths, and were each swept across 100-180

MHz, with a step of 1 MHz. The coils were simulated in air, since the computational load is reduced with lower relative permittivity values. The resonant length, therefore, is greatly increased. The length of the wire is a proxy for wavelength, and with increasing lengths, the resonant frequency reduces. A demonstration of this can be seen in Fig. 2.2 (a).

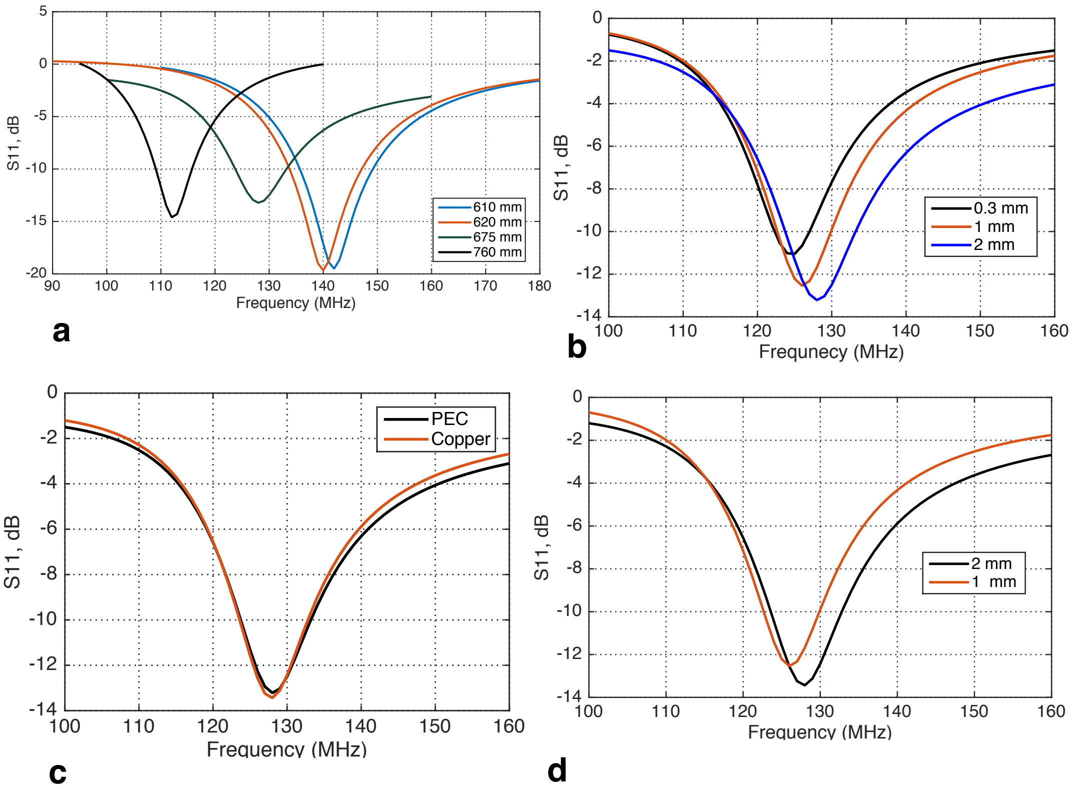

Figure 2.2: Reflection coefficients (S11) as a function of frequency for different loopless coil lengths in air (a) with a diameter of 2mm modeled using PECs. S11 for PEC coils with different diameters can be seen in (b). Additionally, S11 comparisons of PEC and copper (2 mm) as well as 1 and 2 mm diameter copper coils (c,d) are included.

It is also worthwhile to see how S11 changes with different wire diameters, using PECs. This can be seen in Fig. 2.2 (b). Notice how with increasing diameter, the resonant frequency increases. This is because of the reduced capacitance with increasing diameter. S11s for PEC and copper conditions are compared with a diameter of 2mm in Fig. 2.2 (c). And finally, S11s of copper coils with 1 and 2 mm diameters are compared (Fig.2.2 (d)). The copper condition has little effect for our application.

Notice in Fig. 2.2 how the power drops are around -20 dB. The resonant structure should be around -30 dB, with greater than 99% power transmission. The standard lumped port impedance is set to 50 ohm, which is the standard load impedance that must be matched. In order to match this frequency on the bench, a tuning/matching circuit is used, and placed outside of the scanner. However, for the simulations, we can just sweep across a range of impedance values, until we reach a minimum for the S11 parameter. Then, a final sweep over a range of frequencies can be done. Another way to do this would be to simulate the impedance of the resonant structure, and then match the port impedance accordingly.

2.3 Transmission Line coil

As discussed, the coil geometry for the transmission line simulation consists of a coaxial cable measuring a quarter wavelength, with a single turn, shorted loop at its distal end. The coil was simulated in pure water. At the point in time in which the this simulation was run, inclusion of more realistic physiological sample loading conditions had not been developed.

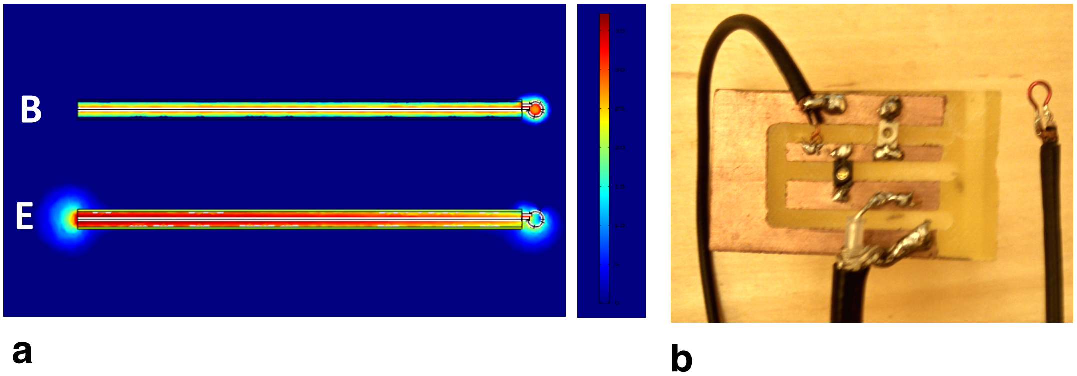

Figure 2.3: Electric and Magnetic simulation maps of the Transmission line coil (a) and a built prototype with the tuning/matching circuit (b). Max values are in red and min values are blue.

The strong magnetic field and relatively small electric field in the vicinity of the single turn loop is what we would expect from the transmission line coil (Fig.2.3 (a)). We also built a prototype with a tuning/matching circuit, which tunes the coil to the resonant frequency of 128 MHz and matches the impedance to 50 ohms. One of the capacitors is fixed and the other is tunable (variable). The outer braid acts as a ground plane. The two capacitors are aligned in series. An image of the very rough prototype can be seen in Fig. 2.3 (b). The prototype has a much larger diameter coaxial cable than what would be used in animal experiments, and the shorted loop would be contained within the diameter of the cable. Coaxial cables as small as 0.3 mm in diameter could be used.

2.4 Loopless coil

The following simulations are of the loopless coil, measuring again, roughly a quarter wavelength with sample loading conditions described in section 2.2. It was realized that COMSOL uses an opposite sign convention for the imaginary component of the permittivity, after running a preliminary time dependent study to measure the temperature change in the immediate vicinity of the coil. The region cooled down instead of heating up. The simulations shown in this section were conducted prior to this realization. The effect of this error in sign convention is explained in more detail for each simulation.

As discussed, finding the resonant frequency of the coil is of primary importance for proper assessment of performance. If the driving AC voltage is detuned from the operating frequency of the probe, then propagation of the voltage wave on the coil will be prevented with varying extents, depending on the magnitude of the detuning. The effect of different voltage detuning frequencies on the magnetic and electric fields produced by the coil can be seen in Fig.'s 2.4 and 2.5, with the resonant case of 128 MHz highlighted with a black border.

The magnetic field is dramatically reduced for detunings below the resonant frequency. The

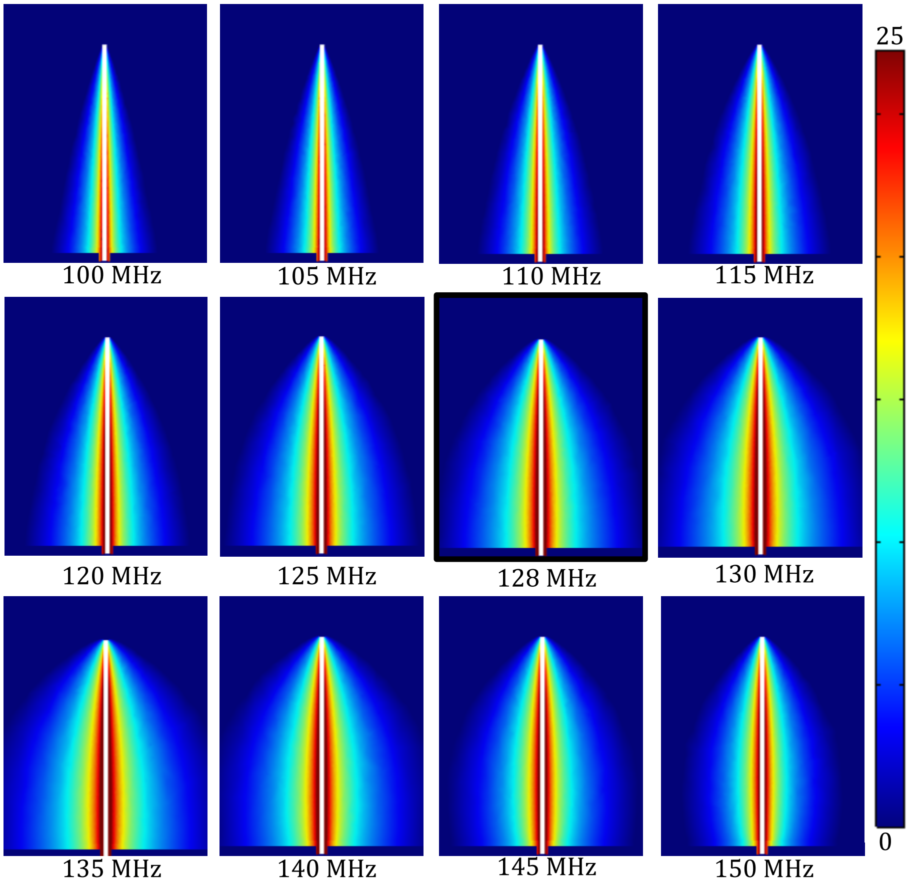

Figure 2.4: Parametric sweep across frequencies, showing the magnetic field distributions (log scale). Large detuning frequencies prevent EM wave propagation on the structure. The resonant frequency of 128 MHz is highlighted in black.

magnetic field is produced by the current flow. Some current will flow even in the highly detuned cases. For the lower detuning, the voltage wavelength is larger than the coil length. This results in a large impedance mismatch, and the wave mostly reflects back. As the detuning frequency approaches the resonant frequency, the electric field distribution maximizes at the distal tip and minimizes at the proximal end. Beyond the resonant frequency, the voltage wave is shorter than the coil length. This causes the electric field node to ascend the length of the coil with frequencies greater than the resonant mode.

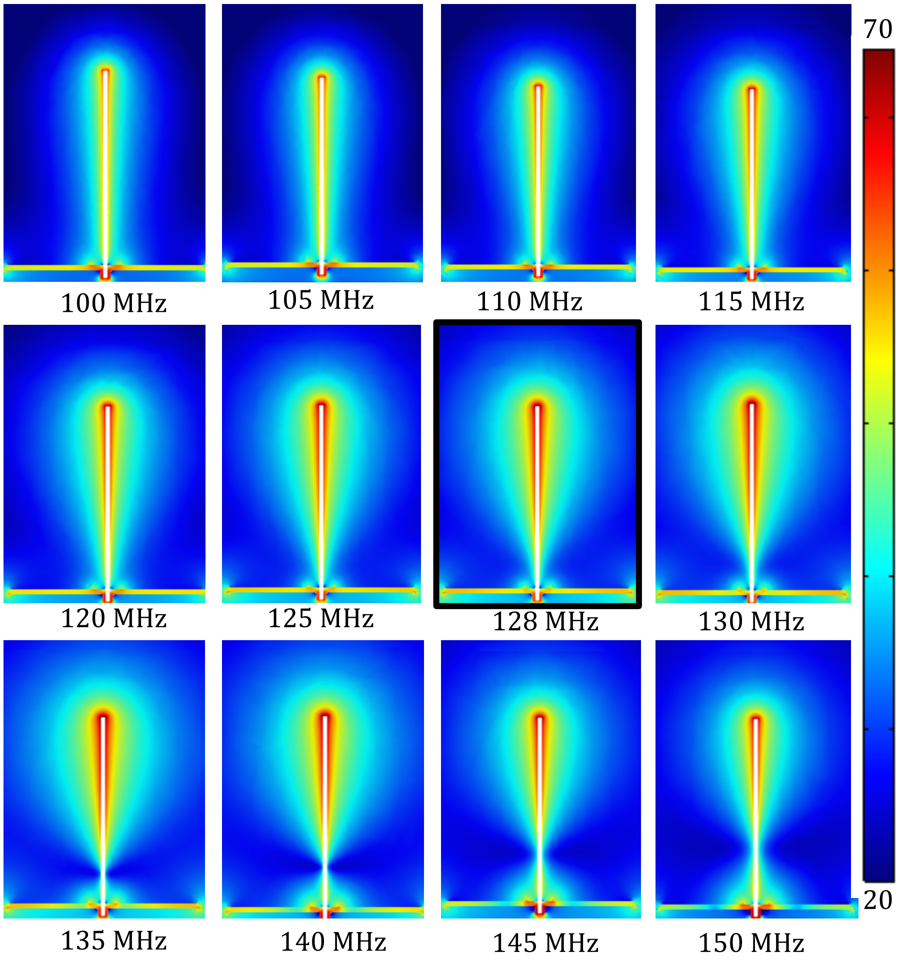

Figure 2.5: Electric field distributions (log scale) as a function of frequency, demonstrating the effects of detuning. The resonant frequency of 128 MHz is highlighted in black.

2.4.1 Dielectric Coating

In order to reduce the large electric field produced at the distal end of the loopless coil, a dielectric coating can be used. Adding a dielectric coating, as discussed, is essential, since charge will leak into the surrounding conductive tissue. The resonant length of the bare coil is 74 mm under sample loading conditions. We would actually expect the resonant pole length to be shorter than this for 3T MRI. This longer length is a result of the opposite sign convention of the permittivity, as mentioned, and is also due to the small simulation domain. We also add a uniformly distributed 0.2 mm thick dielectric coating to the outer surface of the coil. The dielectric material is defined with a relative permittivity of 1000, relative permeability of 1, and an electrical conductivity of 0 S/m. This increases the total diameter to 2.6 mm, and decreases the length to 68.8 mm. The electric and magnetic field maps of the bare and insulated coils can be seen in Fig. 2.6 (a). These maps are not on a log scale, as in Fig.'s 2.4 and 2.5. The signal obtained is proportional to the magnetic field and the noise is associated with the electric field. A quick estimate of the SNR was obtained by dividing the magnetic field norm by the electric field norm, similar to what is done in [30]. It does not make sense to assign absolute numerical values for the SNR using this method, but mapping this B/E quantity can give a picture of the expected imaging coverage and relative regional SNR.

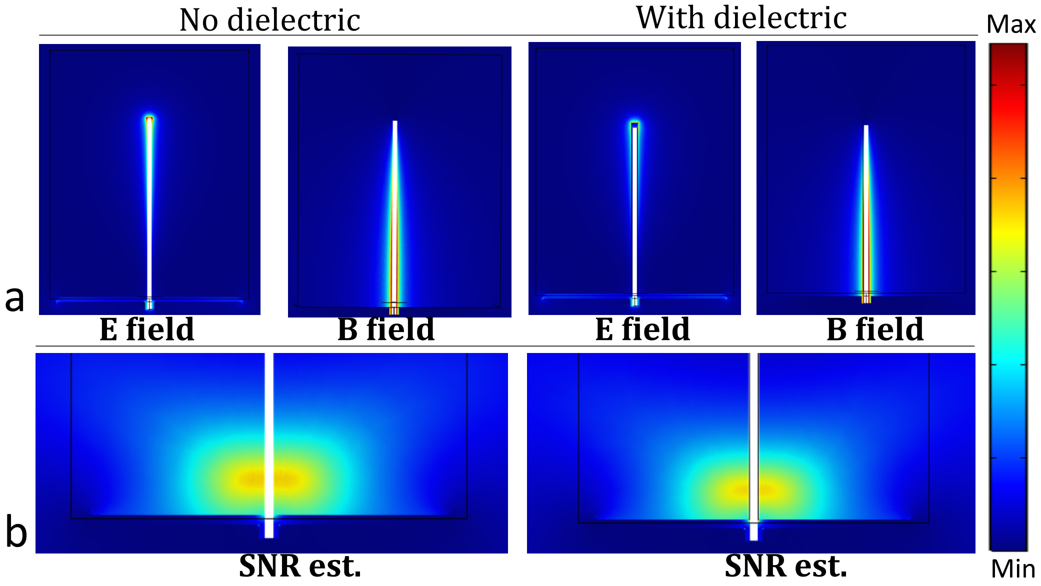

Figure 2.6: Numerical simulations of the electric (V/m) and magnetic (A/m) fields are mapped in (a). The data ranges from 0-3495 V/m and 0-27 A/m and 0-25 A/m for the cases with and without dielectric coating. Values for the estimates of SNR (b) are arbitrary.

Line profiles of the electric field 0.1 mm beyond the distal tip of the probe, with and without dielectric coating show the extent to which the electric field can be mitigated (Fig.2.7 (a)). The corners are hot spots, with the bare coil reaching a maximum of 5000 V/m at its distal end. The electric field at these hot spots is reduced to around 3600 V/m. The electric field at a distance 3 mm from the coil axis is greater for the dielectric case. This may be because the dielectric alters the charge mobilization over the conducting surface. The simulated reflection coefficients can be seen in Fig. 2.7 (c).

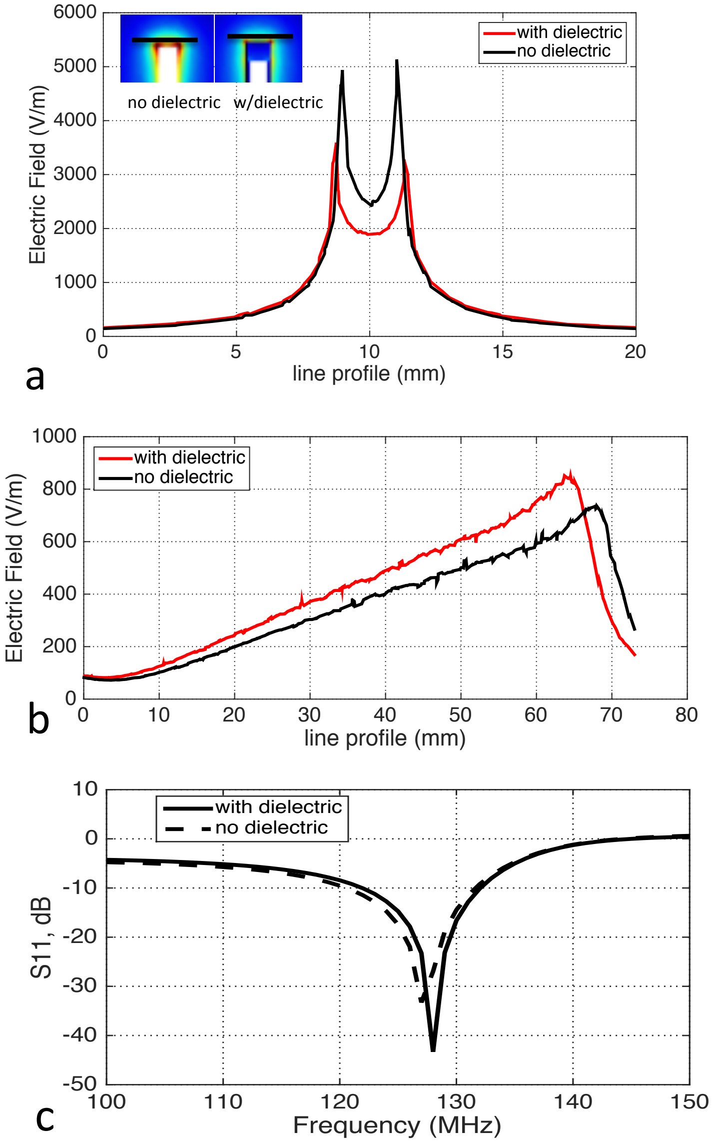

Figure 2.7: Line profiles of the electric field can be seen in (a) and (b) with the latter being along the axis of the coil at a distance of 3 mm. Numerical simulations of the reflection coefficients (c) (S11, dB) ensure that our coils are operating at the resonant frequency.

We were able to adequately assess the capabilities of a loopless coil with and without a high dielectric coating in this proof of concept study. Although the dielectric coating reduces noise resistance at the tip of the coil, the electric field at a distance of 3 mm from the axis is increased, and the SNR is reduced. Further iterations could be done with different distributions of dielectric coating, as well as with different permittivity values up to 3000 [31].

2.5 Corkscrew Inductive Loop

After being acutely aware of the importance of regaining signal at the end of the loopless coil, more attention was given towards coming up with a solution. Using the FEM software gives the user the ability to look at the device from a different perspective, and easily build and test prototypes in a much quicker and resourceful fashion than building and testing on the bench. With nearly 20 years since the invention of the loopless coil, relatively little progress has been made in the visualization of its tip. With this in mind, the corkscrew inductive loop is proposed to address this issue.

COMSOL allows one to easily build a helical structure. It is one of the 3D shape 'options.' The corkscrew shape is unconventional, and it took 4 carefully shaped custom segments to make the loop. There are several reasons why this shape was used. The loop must be self contained within the diameter of the coil (2mm in this case) and the loop must be long enough and have enough turns to produce a large enough electromotive force. Also, the diameter of the wire should not be so small that losses and heating become major factors. A simple helix or solenoid would extend beyond the length of the diameter of the coil. The corkscrew contains roughly 1.6 turns, with a total length of about 9 mm. One end of the corkscrew was "soldered" to the distal end of the loopless coil. The coil diameter is 2 mm and the corkscrew loop sits over the distal end and an open circuit is maintained. The axis of the inductive loop sits in a slightly skewed xy plane. This is important, because signal can be obtained even if the probe is navigated through tortuous vasculature unaligned with the bore of the scanner, as long as the catheter is not rotated.

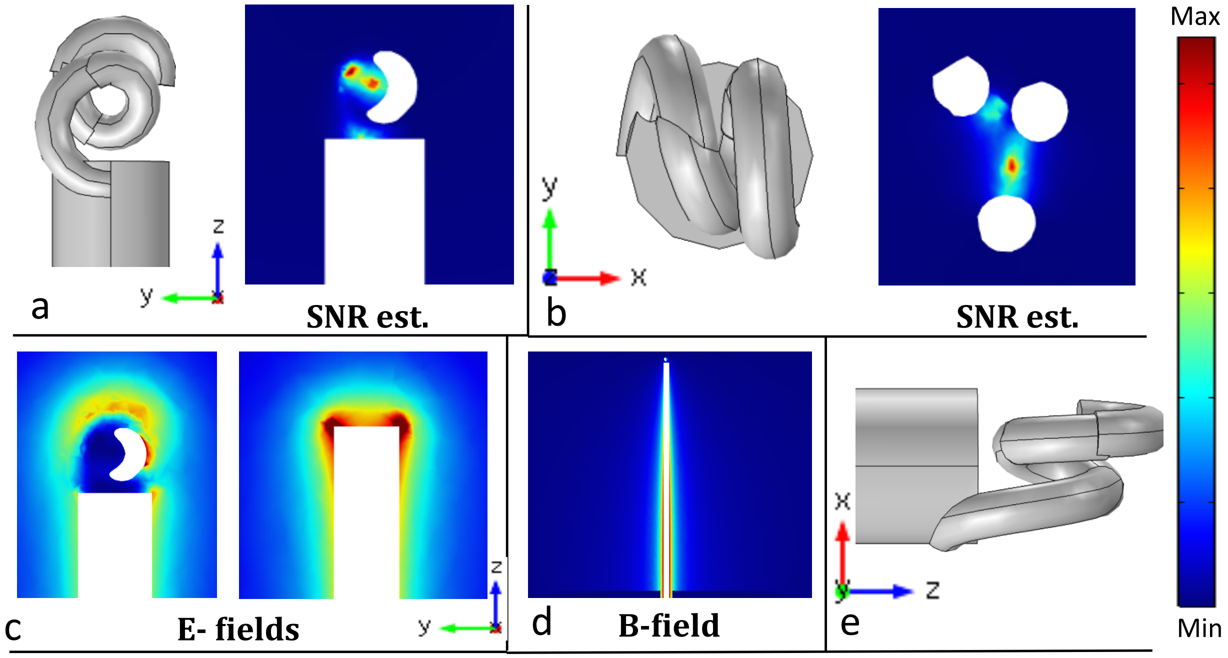

Figure 2.8: The corkscrew geometry and SNR estimates for two different views (a,b) indicate signal recovery where it is needed most. The electric field from the lowest section of the corkscrew cancels with the electric field from the end of the antenna (c), allowing for signal gain in the axis of the loop. The magnetic field along the length of the loopless coil is shown in (d). A side view of the corkscrew is included for completeness (e). Absolute values for the simulation results are not important for this study.

The strong electric field produced at the distal end of a bare coil (no corkscrew) is shown in the right pane of Fig. 2.8 (c). The electric void created by the added corkscrew allows for generation of signal from the induced magnetic field (Fig. 2.8 (a,b)) . Simulations were run after adding each segment. Signal recovery was only observed with the addition of the final segment. The high signal recovery region shown in Fig. 2.9 is roughly 1.2 mm^3. The simulation results shown here were conducted with the opposite sign convention for the permittivity of blood. The simulations were re-run with the appropriate sign convention and the signal gain in the loop is nearly double in magnitude. Partial volume averaging could be an issue depending on the imaging parameters. Since the signal gain is shown to be highly elevated (with simulations) in the region of the corkscrew, even partial volume averaging over several voxels might not completely wash out the signal.

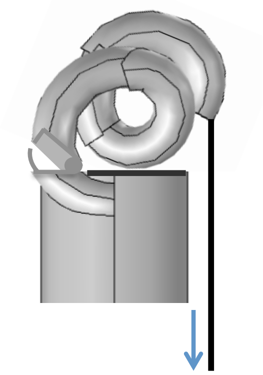

Figure 2.9: A possible design consideration for regaining SNR along the imaging portion of the coil, with a hinged corkscrew attached to a non-metallic pull wire.

The performance of the imaging portion of the coil is reduced with the addition of the loop, since the the added inductive structure alters the quarter wave electromagnetic configuration. The inductive loop induces current flow in a region of the coil which previously had none. This problem could be resolved by putting the corkscrew on a hinge, and attaching the end of the loop to a mechanical pull wire [32], seen in Fig. 2.9. The downward facing direction of the final segment is convenient for the mechanical switch design. At the outer diameter of the probe, where the corkscrew lifts off the distal end of the tip, a dielectric shield should be placed to protect the vessel from being pinched. The pull wire could hug the length of the imaging coil and the catheter, and be placed inside a protective outer insulation. To lift the corkscrew off of the base of the distal end of the probe, the pull wire would only need to be moved downward by about 0.4 mm. This very small displacement may require an electrical actuator.

2.5.1 Specific Absorption Rate of the Corkscrew

We would expect that adding an inductive loop made up of a small diameter wire would increase power deposition to the tissue. The SAR of the loop was studied for wire diameters of 0.6 mm and 0.2 mm and compared with the bare coil. The SAR for each scenario is mapped in an xy plane 0.1 mm above the tip of the bare coil and corkscrews. We should note that the SAR values are shown only to compare the relative differences for the different cases. This is because the magnetic field amplitude generated by the coil has not been calibrated for a 90^0 flip angle for a typical rectangular pulse lasting three microseconds. This would require a magnetic field on the order of two microtesla within the imaging region [33, 34]. This is definitely not the case for a 1V supply. We stress the relative SAR values for each scenario. The SAR of a bare coil has been studied elsewhere and has shown to be safe at normal operating conditions [35], and thus, is used as a reference for the corkscrew cases shown here.

The three SAR planes can be seen in Fig. 2.10 (b, c, d). Line profiles of the SAR across the planes are shown in Fig. 2.10 (a). The bare probe has a circular region with a 3 mm diameter over which there is an elevated SAR. The 0.6 and 0.3 mm diameter corkscrews have a smaller elevated SAR region. The max increase for the 0.6 mm loop in SAR is about 25% greater than the max for the bare coil. The max increase in SAR for the 0.3 mm diameter loop is nearly 95% more than the bare coil.

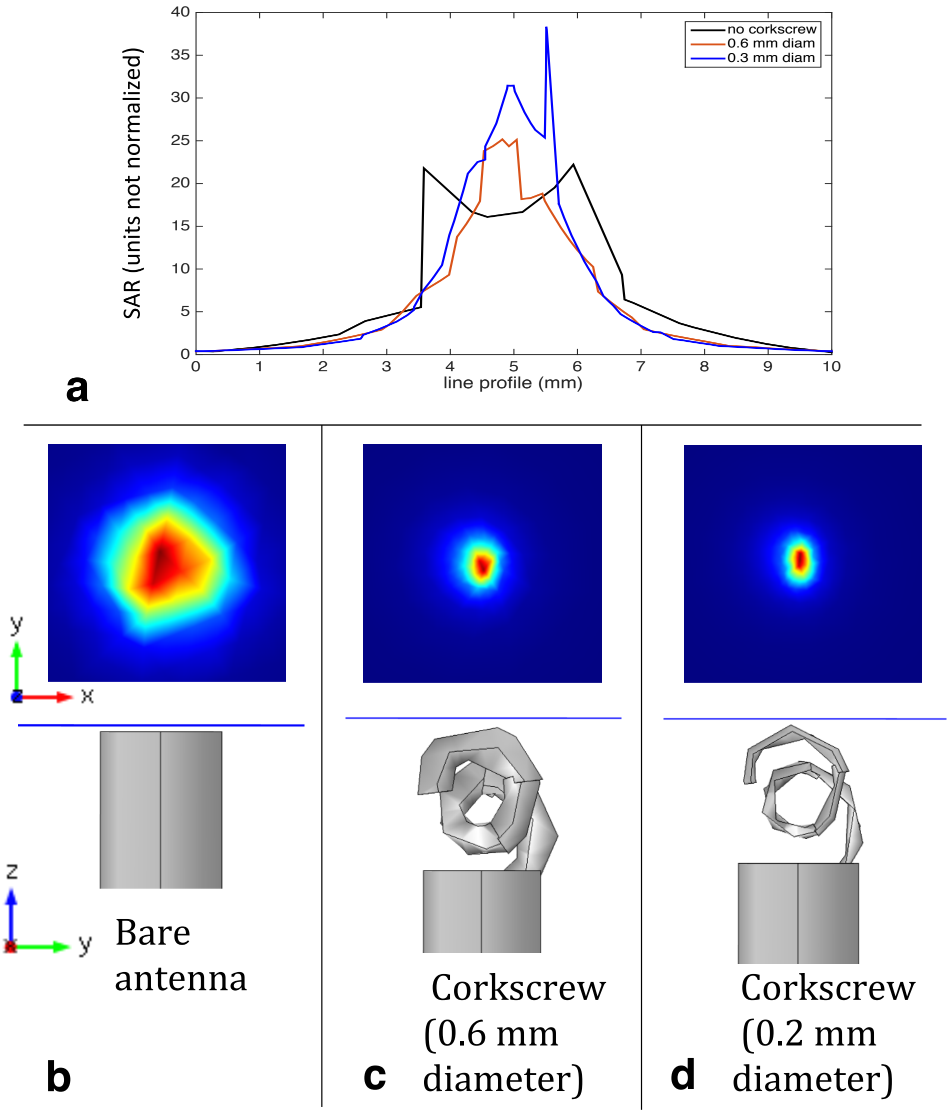

Figure 2.10: The SAR for the case of the bare antenna, a corkscrew with a wire diameter of 0.6 mm, and a corkscrew with a diameter of 0.2 mm, is studied. The SAR is mapped over a 2D plane just north of the tip (0.1 mm above) of the bare coil (b), and corkscrews with different diameters (c, d)

2.6 Discussion

The studies of the loopless coil with extremely high dielectric coating could be redone with the appropriate sign convention of the imaginary component of the permittivity. This is one case which was not retested. This is one limitation of the model. The reruns with the corkscrew using the appropriate sign convention for the permittivity of blood indicate an even higher signal gain within the axis of the loop, as shown in sec. 2.5.

While COMSOL allows for fast computation times, it is limited in its capabilities for including large body components relative to the size of the device. The coil must be finely meshed, since it is a crucial region over which an accurate approximation needs to be obtained. The smaller the coil with respect to the simulation domain, the smaller the finite elements on the coil with respect to the size of finite elements on other domains. This can prevent the simulation from running.

The high signal gain within the axis of the corkscrew could make it a potential active tracking mechanism. Active tracking implies the generation of signal for visualization of devices, as opposed to passive tracking, which is based on signal voids from susceptibility artifacts [36]. The corkscrew could allow navigation and placement of the loopless imaging probe to its target location under MRI guidance. The type of imaging sequence that could be used to track the inductive loop might involve the acquisition of a background reference image obtained with a surface or body coil. This image could be overlaid with an image taken with the corkscrew attached to the loopless coil. The loopless coil would need to be connected to a detuning circuit, so that an emf is not induced in the coil during acquisition of the background reference image. Overlaying these images in rapid succession could be used during navigation of the coil to the vasculature of interest. Since the signal gain is shown to be in a very small region, the distal tip of the loopless coil has the potential to be localized to very high precision. This would allow for navigation of the probe to very small vessels.

Once the loopless coil is in the region of vasculature to be imaged with high resolution, tipping the corkscrew off of the base of the coil using a hinge and mechanical or electrical actuator, as discussed in sec. 2.5, could allow for full recovery of the SNR along the imaging portion of the coil. This development would provide dual functionality for the loopless coil. Many different active tracking mechanisms have been developed [36–39] but few have combined them with endovascular imaging coils. There is one study that stands out as a combined approach for imaging and active tracking [40], which uses two independent solenoid coils wound in opposite directions. This approach is successful, but is rather bulky. The design we propose is compact, taking up no more space than a guidewire. The loopless coil we simulated had a diameter of 2mm. With a developed simulation analysis completed, the next step is to build simple prototypes and see if the corkscrew can generate enough signal to be localized. We could then determine how small of a diameter coil could be used, since the diameter of the coil constrains the size of the corkscrew.

The loopless coil has several advantages over the transmission line resonator–it has an increased imaging coverage and it is compact, making it conducive to endovascular access. The transmission line resonator does have a high, uniform SNR region. However, the size of the imaging region is highly dependent on the size of the loop. This means that access to smaller vasculature will require a smaller loop, and consequently, a smaller imaging coverage. The loopless coil does not have this problem in the imaging portion of the coil, but the corkscrew has an analogous problem. It is constrained in size by its ability to generate a detectable signal, and possibly by its power deposition to surrounding tissue.

2.7 Conclusion

Electromagnetic simulations of endovascular RF probes have been carried out using the Finite Element Method. High dielectric coating is shown to reduce current losses at the distal end of the loopless coil, with reduced SNR along the imaging portion of the probe. A new mechanism for localizing the distal tip of a loopless coil is proposed, based on a corkscrew inductive loop that could be switched ’on’ and ’off’.

References

[1] S. Rudin, D. R. Bednarek, and K. R. Hoffmann, "Endovascular image-guided interventions (eigis)," *Medical physics*, vol. 35, no. 1, pp. 301–309, 2008.

[2] D. Gandhi, J. Chen, M. Pearl, J. Huang, J. Gemmete, and S. Kathuria, "Intracranial dural arteriovenous fistulas: classification, imaging findings, and treatment," *American Journal of Neuroradiology*, vol. 33, no. 6, pp. 1007–1013, 2012.

[3] S. B. King, "The development of interventional cardiology," *Journal of the American College of Cardiology*, vol. 31, no. 4s2, pp. 64B–88B, 1998.

[4] P. Libby, "Atherosclerosis: the new view.," *Scientific American*, vol. 286, no. 5, pp. 46–55, 2002.

[5] R. Ross, "Atherosclerosis—an inflammatory disease," *New England journal of medicine*, vol. 340, no. 2, pp. 115–126, 1999.

[6] P. Libby, "Inflammation in atherosclerosis," *Arteriosclerosis, thrombosis, and vascular biology*, vol. 32, no. 9, pp. 2045–2051, 2012.

[7] P. Libby, "Molecular bases of the acute coronary syndromes," *Circulation*, vol. 91, no. 11, pp. 2844–2850, 1995.

[8] Z. Fayad and V. Fuster, "Clinical imaging of the high-risk or vulnerable atherosclerotic

plaque," *Circulation research*, vol. 89, no. 4, pp. 305–316, 2001.

[9] T. Thom, N. Haase, W. Rosamond, V. J. Howard, J. Rumsfeld, T. Manolio, Z.-J. Zheng, K. Flegal, C. O'Donnell, S. Kittner, *et al.*, "Heart disease and stroke statistics–2006 update: a report from the american heart association statistics committee and stroke statistics subcommittee.," *Circulation*, vol. 113, no. 6, p. e85, 2006.

[10] M. Wintermark, R. Meuli, P. Browaeys, M. Reichhart, J. Bogousslavsky, P. Schnyder, and P. Michel, "Comparison of ct perfusion and angiography and mri in selecting stroke patients for acute treatment," *Neurology*, vol. 68, no. 9, pp. 694–697, 2007.

[11] J. Astrup, B. K. Siesjö, and L. Symon, "Thresholds in cerebral ischemia-the ischemic penumbra.," *Stroke*, vol. 12, no. 6, pp. 723–725, 1981.

[12] M. Wintermark, A. E. Flanders, B. Velthuis, R. Meuli, M. Van Leeuwen, D. Goldsher, C. Pineda, J. Serena, I. Van Der Schaaf, A. Waaijer, *et al.*, "Perfusion-ct assessment of infarct core and penumbra receiver operating characteristic curve analysis in 130 patients suspected of acute hemispheric stroke," *Stroke*, vol. 37, no. 4, pp. 979–985, 2006.

[13] S. Kamalian, S. Kamalian, A. Konstas, M. Maas, S. Payabvash, S. Pomerantz, P. Schaefer, K. Furie, R. González, and M. Lev, "Ct perfusion mean transit time maps optimally distinguish benign oligemia from true "at-risk" ischemic penumbra, but thresholds vary by postprocessing technique," *American Journal of Neuroradiology*, vol. 33, no. 3, pp. 545–549, 2012.

[14] J. Narvid, S. W. Hetts, D. Larsen, J. Neuhaus, T. P. Singh, H. McSwain, M. T. Lawton, C. F. Dowd, R. T. Higashida, and V. V. Halbach, "Spinal dural arteriovenous fistulae: Clinical features and long-term results," *Neurosurgery*, vol. 62, no. 1, pp. 159–167, 2008.

[15] T. R. Beijer, E. J. van Dijk, J. de Vries, S. E. Vermeer, M. Prokop, and F. J. Meijer,

"4d-ct angiography differentiating arteriovenous fistula subtypes," *Clinical neurology and neurosurgery*, vol. 115, no. 8, pp. 1313–1316, 2013.

[16] D. Katritsis and M. Webb-Peploe, "Limitations of coronary angiography: an underestimated problem?," *Clinical cardiology*, vol. 14, no. 1, pp. 20–24, 1991.

[17] E. Larose, Y. Yeghiazarians, P. Libby, E. K. Yucel, M. Aikawa, D. F. Kacher, E. Aikawa, S. Kinlay, F. J. Schoen, A. P. Selwyn, *et al.*, "Characterization of human atherosclerotic plaques by intravascular magnetic resonance imaging," *Circulation*, vol. 112, no. 15, pp. 2324–2331, 2005.

[18] E. M. Haacke, R. W. Brown, M. R. Thompson, R. Venkatesan, *et al.*, *Magnetic resonance imaging: physical principles and sequence design*, vol. 82. Wiley-Liss New York:, 1999.

[19] D. Hoult, "The principle of reciprocity in signal strength calculations—a mathematical guide," *Concepts in Magnetic Resonance*, vol. 12, no. 4, pp. 173–187, 2000.

[20] A. J. Martin, D. B. Plewes, and R. M. Henkelman, "Mr imaging of blood vessels with an intravascular coil," *Journal of Magnetic Resonance Imaging*, vol. 2, no. 4, pp. 421–429, 1992.

[21] R. C. Susil, C. J. Yeung, and E. Atalar, "Intravascular extended sensitivity (ives) mri antennas," *Magnetic resonance in medicine*, vol. 50, no. 2, pp. 383–390, 2003.

[22] O. Ocali and E. Atalar, "Intravascular magnetic resonance imaging using a loopless catheter antenna," *Magnetic resonance in medicine*, vol. 37, no. 1, pp. 112–118, 1997.

[23] H. Yuan, X. Lv, X. Ma, R. Zhang, Y. Fu, X. Yang, X. Wang, Z. Zhang, J. Zhang, and J. Fang, "An intravascular loopless monopole antenna for vessel wall mr imaging at 3.0 t," *Magnetic resonance imaging*, vol. 31, no. 1, pp. 150–155, 2013.

[24] J. T. Vaughan and J. R. Griffiths, *RF coils for MRI.* John Wiley & Sons, 2012.

[25] D. Qian, A.-M. M. El-Sharkawy, E. Atalar, and P. A. Bottomley, "Interventional mri: tapering improves the distal sensitivity of the loopless antenna," *Magnetic resonance in medicine*, vol. 63, no. 3, pp. 797–802, 2010.

[26] J. Mispelter, M. Lupu, and A. Briguet, *NMR probeheads for biophysical and biomedical experiments: theoretical principles and practical guidelines.* Imperial College Press, 2006.

[27] C. Gabriel, "Compilation of the dielectric properties of body tissues at rf and microwave frequencies.," tech. rep., DTIC Document, 1996.

[28] W. B. Zimmerman, *Multiphysics Modeling With Finite Element Methods (series on Stability, vibration and control of systems, serie).* World Scientific Publishing Co., Inc., 2006.

[29] A. C. Polycarpou, "Introduction to the finite element method in electromagnetics," *Synthesis Lectures on Computational Electromagnetics*, vol. 1, no. 1, pp. 1–126, 2005.

[30] R. Rojas and A. O. Rodriguez, "Numerical study of the snr and sar of mri coil arrays," in *2007 29th Annual International Conference of the IEEE Engineering in Medicine and Biology Society*, pp. 1196–1199, IEEE, 2007.

[31] V. Petrovsky, T. Petrovsky, S. Kamlapurkar, and F. Dogan, "Dielectric constant of barium titanate powders near curie temperature," *Journal of the American Ceramic Society*, vol. 91, no. 11, pp. 3590–3592, 2008.

[32] A. Ali, D. H. Plettenburg, and P. Breedveld, "Steerable catheters in cardiology: Classifying steerability and assessing future challenges," *IEEE Transactions on Biomedical Engineering*, vol. 63, no. 4, pp. 679–693, 2016.

[33] C. M. Collins and M. B. Smith, “Signal-to-noise ratio and absorbed power as functions of main magnetic field strength, and definition of “90 °” rf pulse for the head in the birdcage coil,” *Magnetic Resonance in Medicine*, vol. 45, no. 4, pp. 684–691, 2001.

[34] C. M. Collins and M. B. Smith, “Calculations of b1 distribution, snr, and sar for a surface coil adjacent to an anatomically-accurate human body model,” *Magnetic resonance in medicine*, vol. 45, no. 4, pp. 692–699, 2001.

[35] C. J. Yeung, R. C. Susil, and E. Atalar, “Rf safety of wires in interventional mri: using a safety index,” *Magnetic resonance in medicine*, vol. 47, no. 1, pp. 187–193, 2002.

[36] W. Wang, “Magnetic resonance–guided active catheter tracking,” *Magnetic resonance imaging clinics of North America*, vol. 23, no. 4, pp. 579–589, 2015.

[37] H. H. Quick, H. Kuehl, G. Kaiser, D. Hornscheidt, K. P. Mikolajczyk, S. Aker, J. F. Debatin, and M. E. Ladd, “Interventional mra using actively visualized catheters, truefisp, and real-time image fusion,” *Magnetic resonance in medicine*, vol. 49, no. 1, pp. 129–137, 2003.

[38] G. C. Mckinnon, J. F. Debatin, D. A. Leung, S. Wildermuth, D. J. Holtz, and G. K. von Schulthess, “Towards active guidewire visualization in interventional magnetic resonance imaging,” *Magnetic Resonance Materials in Physics, Biology and Medicine*, vol. 4, no. 1, pp. 13–18, 1996.

[39] H. H. Quick, M. O. Zenge, H. Kuehl, G. Kaiser, S. Aker, S. Massing, S. Bosk, and M. E. Ladd, “Interventional magnetic resonance angiography with no strings attached: wireless active catheter visualization,” *Magnetic resonance in medicine*, vol. 53, no. 2, pp. 446–455, 2005.

[40] C. M. Hillenbrand, D. R. Elgort, E. Y. Wong, A. Reykowski, F. K. Wacker, J. S. Lewin, and J. L. Duerk, “Active device tracking and high-resolution intravascular mri

using a novel catheter-based, opposed-solenoid phased array coil," *Magnetic resonance in medicine*, vol. 51, no. 4, pp. 668–675, 2004.

Publishing Agreement

It is the policy of the University to encourage the distribution of all theses, dissertations, and manuscripts. Copies of all UCSF theses, dissertations, and manuscripts will be routed to the library via the Graduate Division. The library will make all theses, dissertations, and manuscripts accessible to the public and will preserve these to the best of their abilities, in perpetuity.

Please sign the following statement:

I hereby grant permission to the Graduate Division of the University of California, San Francisco to release copies of my thesis, dissertation, or manuscript to the Campus Library to provide access and preservation, in whole or in part, in perpetuity.

Author Signature

9/7/2016

Date